Electrical, dielectric and photocatalytic properties of Fe-doped ZnO nanomaterials synthesized by sol gel method

Yacine Cherifi, Ahcène Chaouchi, Yannick Lorgouilloux, Mohamed Rguiti, Abdelaziz Kadri, Christian Courtois

Processing and Application of Ceramics 10 [3] (2016) 125–135
DOI: 10.2298/PAC1603125C

Electrical, dielectric and photocatalytic properties of Fe-doped ZnO nanomaterials synthesized by sol gel method

Yacine Cherifi[1], Ahcène Chaouchi[1,*], Yannick Lorgoilloux[2,3], Mohammed Rguiti[2,3], Abdelaziz Kadri[4], Christian Courtois[2]

[1]*Laboratoire de Chimie Appliquée et Génie Chimique de l'Université Mouloud Mammeri de Tizi-Ouzou, Algérie*
[2]*Laboratoire des Matériaux Céramiques et Procédés Associés – Université de Valenciennes et du Hainaut-Cambrésis, Boulevard Charles de Gaulle, 59600 Maubeuge, France*
[3]*Université Lille Nord de France, F-59000 Lille, France*
[4]*Laboratoire de Physique et chimie des matériaux de l'Université Mouloud Mammeri de Tizi-Ouzou, Algérie*

Received 7 April 2016; Received in revised form 8 July 2016; Accepted 17 August 2016

Abstract

Fe-doped ZnO nanoparticles were synthesized by sol gel technique. Fine-scale and single phase hexagonal wurtzite structure in all samples were confirmed by SEM and XRD, respectively. The band gap energy depends on the amount of Fe and was found to be in the range of 3.11–2.53 eV. The electric and dielectric properties were investigated using complex impedance spectroscopy. AC conductivity data were correlated with the barrier hopping (CBH) model to evaluate the binding energy (W_m), the minimum hopping distance (R_{min}) and the density of states at Fermi level, $N(E_F)$. Fe doping in ZnO also improved the photocatalytic activity. Thus, the sample $Zn_{0.95}Fe_{0.05}O$ showed high degradation potential towards methylene blue (MB), i.e. it degrades 90% of BM in 90 min under UV light.

Keywords: *Fe-doped ZnO, band gap, conductivity, dielectric properties, photocatalytic properties*

I. Introduction

For the last decades, there is an increased interest for zinc oxide (ZnO) because of their wide variety of applications. Zinc oxide is n-type semiconductor [1,2] with a direct large band gap of 3.37 eV [3,4] which is considered as promising candidate for optical and optoelectronic applications in nanoscale devices [5,6]. It is used as a transparent electrode in solar cells [7], chemical and gas sensors [8], spintronic devices [9], and light emitting diodes [10]. ZnO seems also to be a microwave absorbing material and is used as a material in microwave components such as resonators, band pass filters and duplexers [11–13]. Materials with high dielectric constants and low dielectric loss have received special attention due to the rapid developments in microwave telecommunications, satellite broadcasting, discrete and multilayer capacitors, dynamic random access memories and low-loss substrates for microwave integrated circuits [14,15]. Recently, ZnO-based photocatalysts have been successfully used to convert organic pollutants in water into pollutant-free materials through UV light or simulation sunlight [16]. However, the quantum efficiency of ZnO is rather low due to the fast recombination of photoinduced hole-electron pairs [17].

In order to enhance the versatility of ZnO to meet the different requirements of application, structural modifications have usually been utilized, among which metal ion doping is well-known and the most effective approach [18–20]. For example, cobalt (Co) doping can increase the band gap [19], whereas zirconium (Zr) doping can decrease the band gap [21]. ZnO is well-known as n-type semiconductor where its electrical conductivity is due to the excess of zinc interstitial position [21]. Also, ZnO doped with Cr, Mn and Fe has showed novel attention due to the strong correlation between the structural, optical, and magnetic properties [23]. Doping with various amount of Fe^{3+} not only enhances

*Corresponding author: tel: +213 779 357 486,
fax: +213 779 357 486, e-mail: *ahchaouchi@yahoo.fr*

electron-hole pair separation by decrease the band gap to make advantages of shifting the absorption to the visible light spectrum, but also decrease the average grain size [24,25]. As reported in the literature, the presence of more than one valence states on transition metal ion suggests that polaronic conduction is attributed to a hopping mechanism of electrons from low valence state to the high valance one [26–28]. In addition, a unique feature of nanostructures is the large surface to volume ratio available in these systems. They consist of grains, grain boundaries and grain interfaces which play important role in the determination of the electrical properties [29,30]. It is also well-known that the interior defects such as A-site vacancies, space charge electrons or oxygen vacancies have great influence on electrics, dielectrics and optical properties, and they are very important to gain a fundamental understanding of these properties.

In this study, we have used Fe doping to improve the optical and electrical properties of ZnO material. In fact, Fe ion can be easily substituted on the Zn-site, resulting in two more free electrons to contribute to the electrical conduction. Here we report synthesis of ZnO nanostructures, prepared by a polymeric complex method using inexpensive metal nitrate precursors and starch used as the complex agent. Impedance spectroscopy (IS) is considered to be a powerful tool for analysing the electrical properties of material. By changing the applied frequency of the system, different contributions of the electrodes, grain boundaries and individual grains can be distinguished [31,32]. Thus, the effect of Fe addition on the electrical, dielectric, optical and photocatalytic properties of ZnO nanomaterial were also investigated.

II. Experimental

All precursor materials were of analytical grade and used without any purification. Zinc nitrate hexahydrate $Zn(NO_3)_2{\times}6H_2O$ and starch from (corn) were purchased from Sigma-Aldrich, iron (III) nitrate ($Fe(NO_3)_3{\times}9H_2O$) was purchased from Merck (Germany).

To prepare 5 g of Fe-doped ZnO nanopowders ($Zn_{1-x}Fe_xO$, with $x = 0$, 0.02 and 0.05), we dissolved stoichiometric amounts of zinc nitrate ($Zn(NO_3)_2{\times}6H_2O$) and iron nitrate ($Fe(NO_3)_3{\times}9H_2O$) in 50 ml of distilled water under agitation for 30 min, and also 10 g of starch in 150 ml of distilled water under stirring for 30 min at 75 °C. Then, the zinc and iron nitrate solutions were added to the starch solution under stirring in a bath of silicone oil at 80 °C. The agitation was continued for 22 hours to obtain a clear brown resin. The obtained resin was then dried in an oven for 3 hours and heat treated at different temperatures (450 °C, 600 °C and 800 °C) for 5 hours to obtain the Fe-doped ZnO nanopowders (Fig. 1).

To prepare ceramic pellets, the obtained powders were pressed into cylindrical disks (7 and 13 mm in diameter, 1 mm and 1.5 mm thickness) by uniaxial pressing under 60 MPa. The green samples were finally sintered in air at 600 °C for 2 hours, with heating and cooling rates of 150 °C/h.

Structure of the prepared samples was confirmed by FTIR spectra analysis in the range of 400–4000 cm^{-1} using FTIR8400 spectrophotometer-Schimadzu. The crystallised phase composition has been identified by X-ray diffraction (Philips X' Pert) technique using the Cu$K\alpha$ X-ray radiation. The microstructures were observed

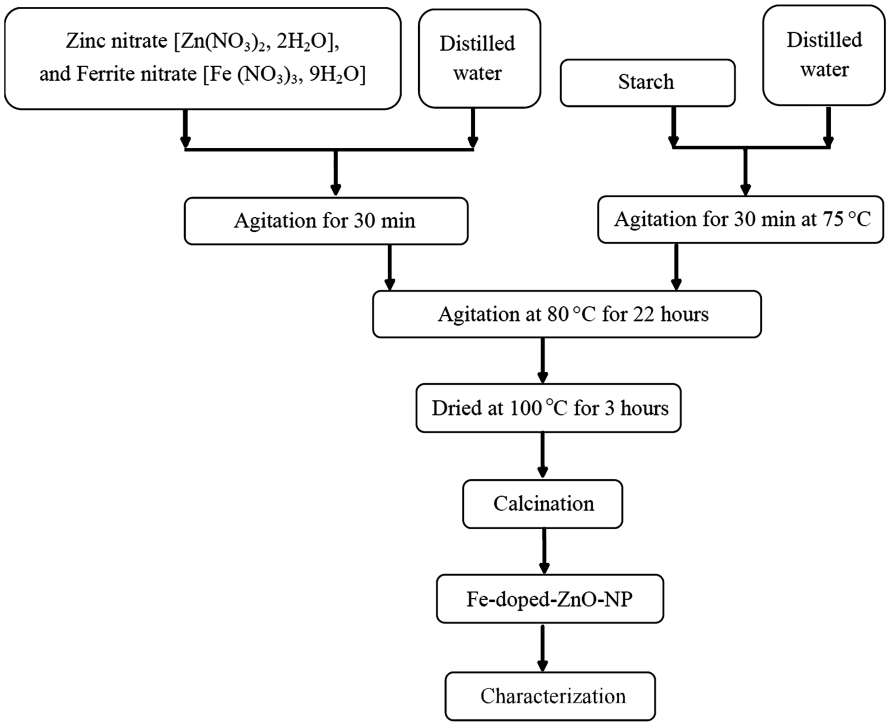

Figure 1. Schematic flow chart of the synthesis of Fe-doped ZnO nanopowders

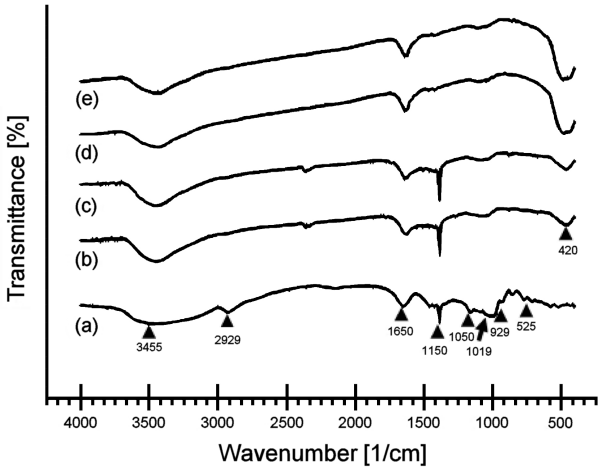

Figure 2. FTIR spectra of starch (a), ZnO dried gel (b) and samples calcined at 450 °C (c), 600 °C (d) and 800 °C (e)

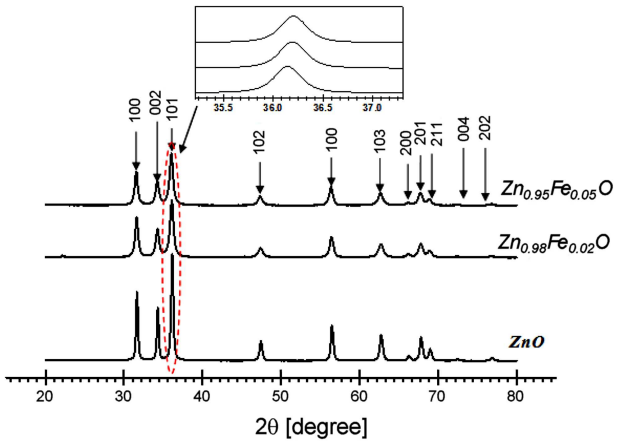

Figure 3. X-ray diffraction patterns of: a) ZnO, b) $Zn_{0.98}Fe_{0.02}O$ and c) $Zn_{0.95}Fe_{0.05}O$

using a scanning electron microscopy (SEM Philips XL'30). The specimens were polished and electroded with a silver paste. The optical properties of the samples dispersed in water with concentration of 0.1 wt.%, were studied using UV-visible spectrophotometer-Schimadzu UV2450. The dielectric and electric properties were determined by using HP4284A meter versus temperature (from 20 °C to 100 °C), and the frequency range from 100 Hz to 1 MHz. The photocatalytic activity of Fe-ZnO nanopowders was tested by decolourization of methylene blue (MB) in aqueous solution at ambient temperature under UV light illumination in a cylindrical Pyrex glass crystallizer. The UV-light source was a high-pressure UV mercury lamp with wavelength of 365 nm and power of 125 W. 30 mg of Fe-ZnO photocatalysts was added to 30 ml MB aqueous solution (20 mg/l), then maintained in darkness for 30 min with magnetic stirring to reach the adsorption-desorption equilibrium. Analytical samples were taken from the suspension in period of 90 min every 15 min, under UV light. The photodegradation efficiency was detected by measuring the absorption at 660 nm using a UV-vis spectrometer.

III. Results and discussion

3.1. Microstructural characterization

Figure 2 shows the FTIR spectra of the starch, dried gel and ZnO samples calcined at 450 °C, 600 °C, and 800 °C. The main absorption bands of the starch can be observed (Fig. 2a) at 1150 cm^{-1}, 1019 cm^{-1} and 1082 cm^{-1} correspond to the C–O–H, C–O–C groups, at 3455 cm^{-1} due to the O–H stretching mode [29] and at around 2930 cm^{-1} corresponding to the elongation of the CH_2 groups. The results of FTIR prove that the atomic bonds of the starch are changed during the sol gel process.

The FTIR transmittance spectra of the samples calcined at different temperatures are shown in Fig. 2. A new absorption peak identified at 1650 cm^{-1} corresponds to the C=O normal stretching vibration mode. The observed large peaks that appeared at 420 cm^{-1} can be attributed to ZnO hexagonal vibration modes [33,34].

Figure 3 shows the X-ray diffraction (XRD) patterns of the heat treated samples. All detectable peaks can be indexed to hexagonal wurtzite structure with space group (*P63mc*) for the pure and doped ZnO samples (confirmed with PDF Card: 00-036-1451 for wurtzite structure). Diffraction spectra show that all samples are in single phase and there are no anomalous peaks related to Fe metal clusters or Fe oxides secondary phases. The observed X-ray diffraction peaks of the doped ZnO are larger than the undoped ZnO and the peak positions shift to higher angle. These could be attributed to the minute amount of Fe^{3+} dopant and the good dispersion of Fe^{3+} into the ZnO lattice [35,36].

The calculated values of crystallite sizes of different samples are presented in Table 1. It can be observed that the crystallite size of ZnO decreases from 20.12 nm to 17.8 nm when Fe content increases from 0 at.% to 5 at.%, indicating that the Fe-doping inhibited the crystallization of ZnO samples. Moreover, the lattice parameters and cell volume decrease with the increase in Fe content. This indicates that Fe^{3+} ions are incorporated into the lattice substituting Zn^{2+}. This phenomenon can be assigned to the difference of the ionic radii of Fe^{3+} (r_i = 0.067 nm) and Zn^{2+} (r_i = 0.083 nm) [37,38]. XRD patterns also exhibit that as the Fe content increases,

Table 1. Cristallite size and lattice parameters of Fe-doped ZnO nanopowders

Fe concentration [at.%]	Crystallite size [nm]	Lattice parameter		Unit cell volume
		a [Å]	*c* [Å]	[Å^3]
0	20.12	3.2490	5.2070	47.70
2	18.8	3.2481	5.2064	47.66
5	17.8	3.2478	5.2060	47.62

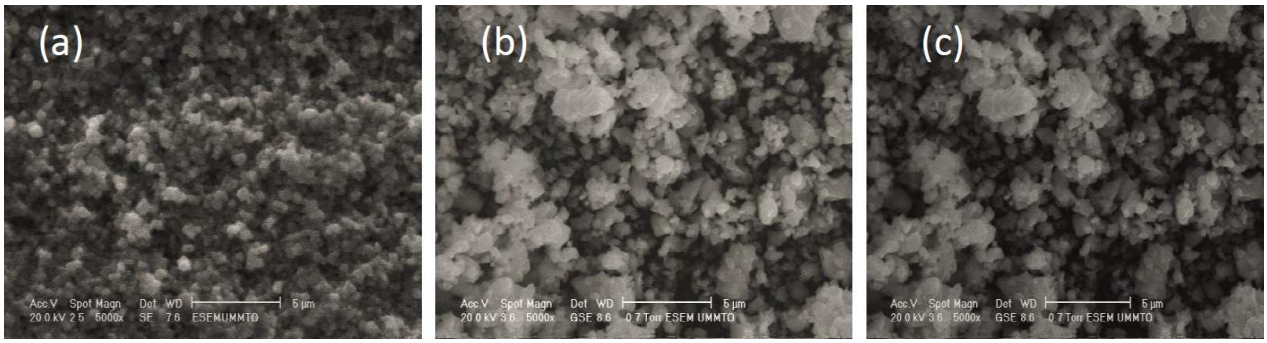

Figure 4. SEM micrographs of fracture surfaces: a) ZnO, b) $Zn_{0.98}Fe_{0.02}O$ and c) $Zn_{0.95}Fe_{0.05}O$

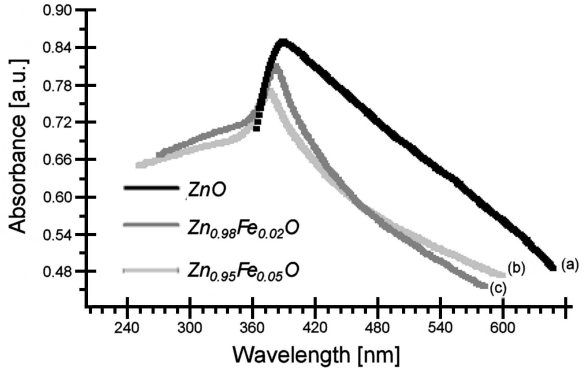

Figure 5. Absorbance spectra of pure and Fe-doped ZnO nanopowders

the intensity of XRD peaks decreases and FWHM increases. This means that Fe-doping in ZnO produces crystal defects around the dopants segregating on grain boundaries. This enhances energy barrier which in turn reduces the movement and the diffusion of Zn^{2+} ions and therefore restrain the growth of ZnO grains, confirming that the Fe ions are incorporated into the ZnO crystal lattice without changing the wurtzite structure [39].

Figure 4 shows the SEM micrographs of the undoped and Fe-doped ZnO sintered at 600 °CÀ slight decrease in particle size of the Fe-doped ZnO compared to the pure ZnO can be seen. The mean crystallite size (d) was calculated from the 101 diffraction peak by the Scherrer formula [40]:

$$d = \frac{k \cdot \lambda}{\beta \cos\theta} \tag{1}$$

where $k = 0.9$, $\lambda = 1.5405$ Å, θ is the Bragg's angle and β is the full width at half maximum (FWHM) of the preferred orientation plane. The mean crystallite size along the (101) plane decreased as the Fe ion content increased (Table 1). This also confirms the influence of doping on the crystallization process [41].

3.2. Optical properties

The UV-vis spectra of the undoped and Fe-doped ZnO are shown in Fig. 5. The first one has a peak absorption at 368 nm which can be attributed to the transition of electrons from the valence band to the conduction band of ZnO ($O_{2p} \longrightarrow Zn_{3d}$) [42,43]. Addition of Fe ions shifted this peak to 376 nm. This red shift observed at the edge of the absorption spectrum is a clear indication of the Fe incorporation into the ZnO matrix. The red shift may occur due to the strain caused by Fe-doping and the change in the band structure of ZnO [44].

The optical band gap is determined by the Tauc relation between the optical absorption coefficient α and the incident photon energy $h \cdot \nu$ [45,46]:

$$\alpha \cdot h \cdot \nu = A(h \cdot \nu - E_g)^n \tag{2}$$

where A is a constant, E_g optical band gap of the material and the exponent n depends upon the type of transition. The n values for direct allowed, indirect allowed and direct forbidden are 1/2, 2 and 3/2, respectively. In the present case, $n = 1/2$ where α is absorption coefficient given by:

$$\alpha = \frac{(1 - R')^2}{2R'} \tag{3}$$

where $R' = R/100$.

The energy band gap of the Fe-ZnO nanoparticles are estimated by plotting $(\alpha \cdot h \cdot \nu)^2$ versus $h \cdot \nu$ as shown in Fig. 6. The extrapolation of the straight line to the energy $(h \cdot \nu)$ axis gives the band gap of the material. The observed energy gap of the Fe-ZnO nanoparticles is decreased from 3.11 to 2.53 eV when Fe concentration is increased from 0 at.% to 5 at.%. In this region, more charge carriers are created by Fe-doping which induces the absorption and reduce the band gap. The variation of the band gap edge for Fe-doped ZnO was also reported by earlier works [47].

3.3. Dielectric properties

Dielectric constant (ε') and dielectric loss ($\tan\delta$) of the undoped and Fe-doped ZnO samples versus frequency are shown in Figs. 7 and 8, respectively. The dielectric properties of a solid material in bulk form are very sensitive to the distribution of local electric field in sample. Therefore, the dependence of the dielectric constant and the dielectric loss on temperature and frequency can provide access to useful information on structural changes, transport mechanism and defect behaviour of a solid. Thus, ε' is the real permittivity and describes the stored energy whereas $\tan\delta$ is the imaginary permittivity and describes the energy dissipation.

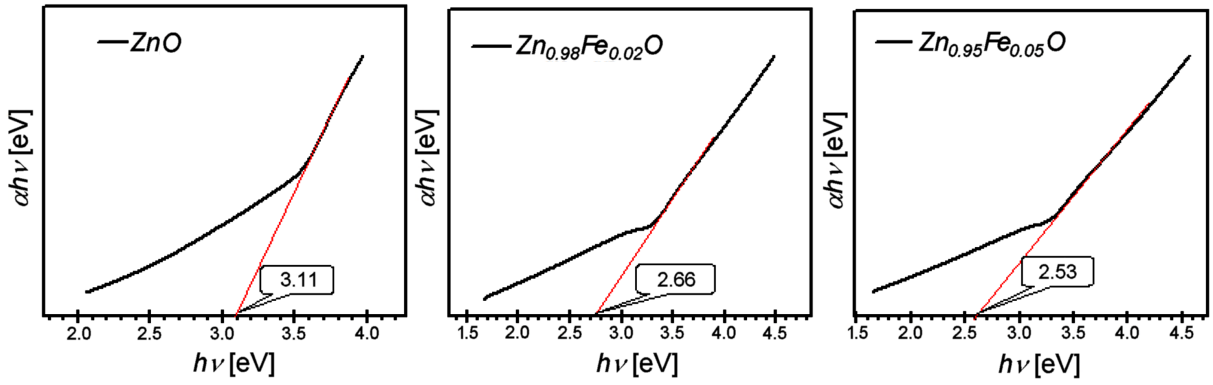

Figure 6. Plot of $\alpha h\nu$ against $h\nu$ in eV for Fe doped ZnO nano-structures

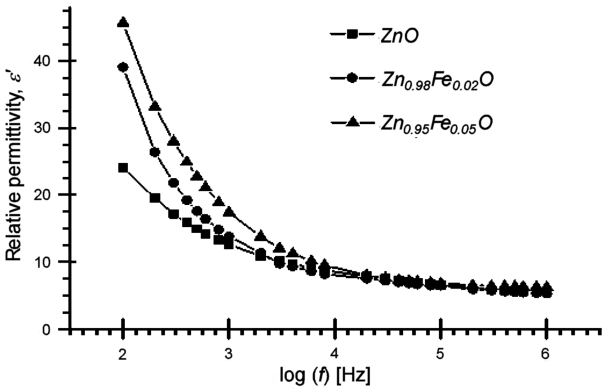

Figure 7. Frequency dependence of permittivity

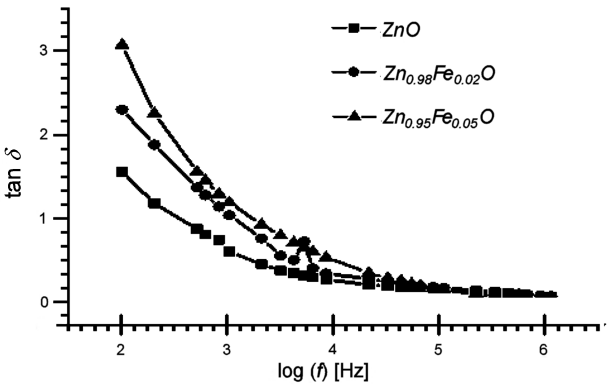

Figure 8. Frequency dependence dielectric loss

Two behaviours can be distinguished for the pure and doped samples (Figs. 7 and 8). Below 10 kHz, the values of dielectric constant and dielectric loss are considered to be high. However, the observed dispersion disappears at high frequencies. It is well known that high values of dielectric constant and dielectric loss for frequencies below 10 kHz are caused by the existence of the space charge in the nanostructure, such as dangling bonds, vacancies and the microspores due to the grain boundaries of their large surface grain. Beyond this frequency, the orientation polarization is the dominant mechanism [48,49]. Furthermore, at low frequencies, the hopping electrons are trapped by these structural inhomogeneities that lead to a dominant space charge polarization in this frequency range. The possible source of orientation polarization is the existence of oxygen vacancies and zinc interstitials in the nano-sized ZnO. When an external field is applied, the Zn ions and the oxygen vacancies in the neighbourhood can change the positions by a single jump and try to align along the direction of field which can be described by the Kröger-Vink notation [50]:

$$\mathrm{Zn_{Zn}} \longrightarrow \mathrm{Zn_i^{2+}} + 2\,\mathrm{e^-}$$
$$\mathrm{O_O} \longrightarrow \mathrm{V_O^{\bullet\bullet}} + 2\,\mathrm{e^-} + \tfrac{1}{2}\mathrm{O_2}$$

However, the value of dielectric constant increases with increasing Fe in ZnO system (Fig. 7). This suggests that Fe ions penetrate at Zn sites as a result of generated electrons by charge transfer ($\mathrm{Fe^{3+}} + \mathrm{e^-} \longleftrightarrow \mathrm{Fe^{2+}}$). On the other hand, the presence of dopant (Fe) increases the number of oxygen vacancies and Zn interstitials in the crystal, which leads to an increase in the dipole moment and, in turn, the orientation polarization. In addition, an increase of dielectric loss is observed with the Fe-doping (Fig. 8), and gradually decreases in the higher frequency domain.

At higher frequencies, the space charges cannot follow the change of the field and hence do not produce space charge polarization. The dipoles are also unable to follow rapidly with varying electric field. Damping of these dipoles accounts for the reduction of dielectric constant at higher frequencies.

3.4. Complex impedance analysis

The complex impedance spectroscopy (CIS) technique is used to analyse the electrical response of polycrystalline samples in a wide range of frequencies and temperatures. The frequency dependent properties of a material can be described as complex permittivity (ε^*), complex impedance (Z^*), complex admittance (Y^*), complex electric modulus (M^*) and dielectric loss or dissipation factor ($\tan\delta$). The real (ε', Z', Y', M') and imaginary (ε'', Z'', Y'', M'') parts of the complex parameters are in turn related to one another as follows:

$$\varepsilon^* = \varepsilon' + j \cdot \varepsilon'' \tag{4}$$

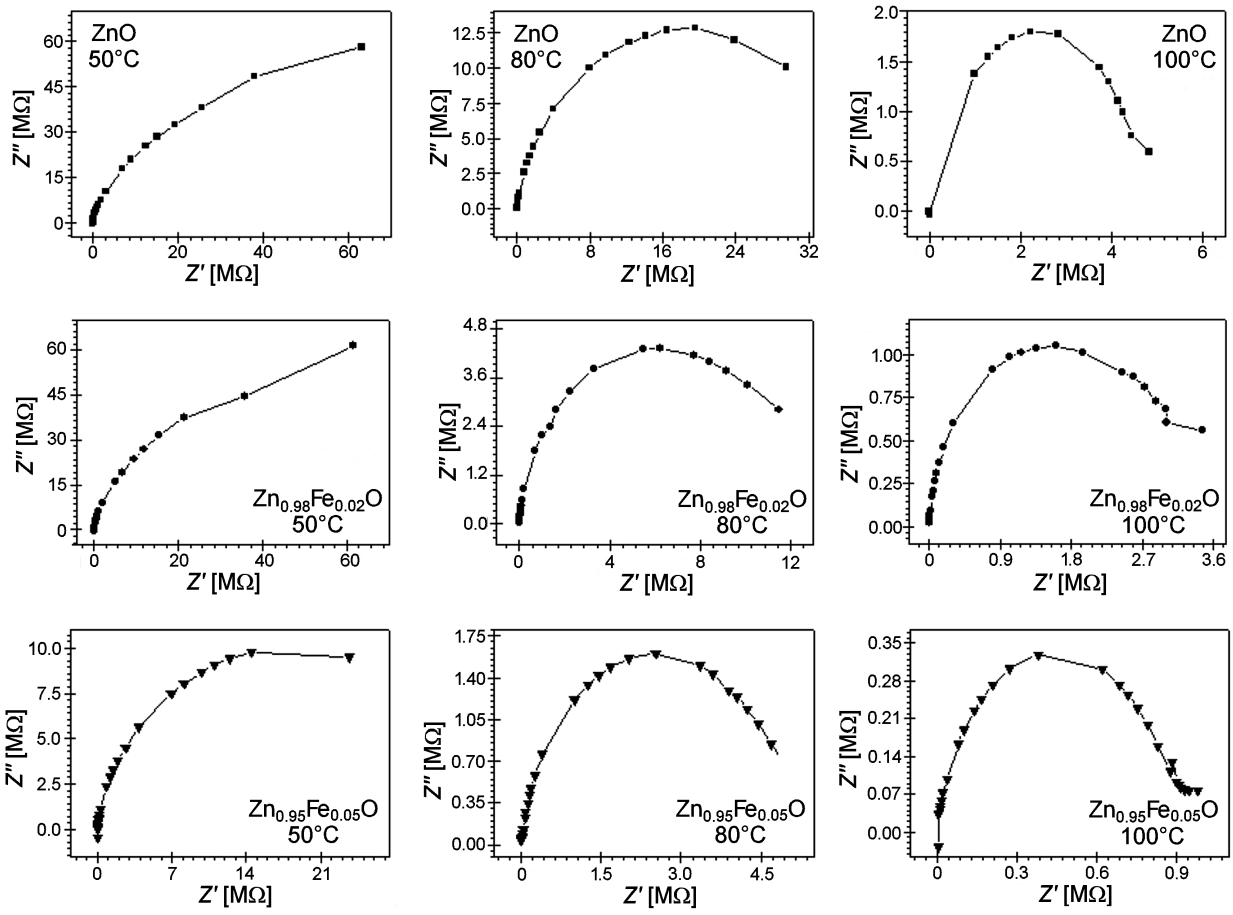

Figure 9. Complex impedance plots (Z'' vs. Z') of undoped and Fe-doped ZnO at different temperatures

$$Z^* = Z' + j \cdot Z'' = \frac{1}{j \cdot C_0 \cdot \varepsilon^* \cdot \omega} \tag{5}$$

$$Y^* = Y' + j \cdot Y'' = j \cdot \omega \cdot C_0 \cdot \varepsilon^* \tag{6}$$

$$M^* = M' + j \cdot M'' = \frac{1}{\varepsilon^*} = j \cdot \omega \cdot \varepsilon_0 \cdot Z^* \tag{7}$$

$$\tan \delta = \frac{\varepsilon''}{\varepsilon'} = \frac{M'}{M''} = \frac{Y'}{Y''} = \frac{Z'}{Z''} \tag{8}$$

where $\omega = 2\pi \cdot f$ is the angular frequency, C_0 is the free geometrical capacitance, and $j^2 = -1$.

Figure 9 shows the temperature dependence of complex impedance spectra (Nyquist plot) of the Fe-doped ZnO over a wide range of frequency from 1 kHz to 1 MHz. These spectra are characterized by the appearance of semicircular arcs, which are temperature dependent. The change in temperature ensures a distinct effect on the impedance characteristics spectra of the material by the appearance of the low temperature single semicircular arc due to the bulk properties of the material and at high temperature (100 °C) the second semicircle begins to form in different studied compositions, due to the bulk and grain boundary conduction. The impedance spectrum in the form of a semicircle is a representation of an electric process which occurs in the material that can be described by means of an equivalent electrical circuit consisting of a combination of resistive and capacitive elements. The high frequency semicircle is attributed to the bulk property of the material (parallel combination of bulk resistance and bulk capacitance), and at the low frequency semicircle is due to the grain boundary effects in the material (parallel combination of grain boundary resistance and capacitance).

3.5. Conductivity studies

AC conductivity of all samples was calculated from the dielectric loss according to the relation:

$$\sigma_{AC}(\omega) = \varepsilon_0 \cdot \omega \cdot \varepsilon'' = \varepsilon_0 \cdot \omega \cdot \varepsilon_r \cdot \tan \delta \tag{9}$$

where $\varepsilon_0 = 8.85 \times 10^{-12}$ F/m is the permittivity of the free space and $\omega = 2\pi \cdot f$ is the angular frequency.

Figure 10 shows the dependence of σ_{AC} conductivity versus frequency for the Fe-doped ZnO samples. A slight increase in conductivity was observed for the Fe-doped ZnO material. This increase can be explained by the increased number of charge carriers derived from either the replacement of Zn by Fe ions or the incorporation of Fe ions in interstitial sites of the ZnO lattice. Thus, the incorporation of Fe ions into the lattice of ZnO crystals leads to the formation of charge carriers through this mechanism involving the replacement of a divalent (Zn^{2+}) cation by a trivalent one (Fe^{3+}) paired with a free

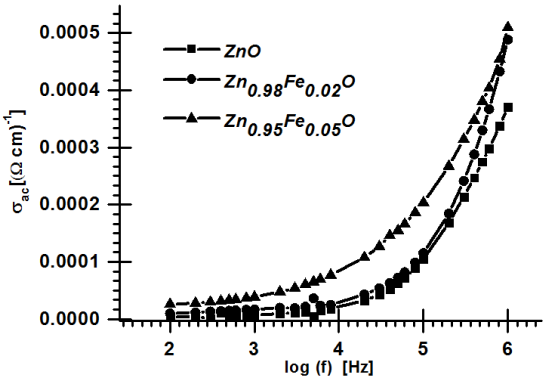

Figure 10. Variation of σ_{AC} conductivity with frequency

electron (e^-), responsible for the increased conductivity. These results are in good agreement with obtained complex impedance spectra (Fig. 9).

It is also remarkable that the frequency dependence of AC conductivity is similar for variety of quite different disordered materials: ionic materials and ionic conducting polymers [51,52]. Conductivity σ_{AC} was found to be frequency independent in the low frequency region and bend off at some critical frequency ω_p. Results for $\omega > \omega_p$ obey the Jonscher's power law equation [53] given by:

$$\sigma_{AC}(\omega) = \sigma_{DC} + A\omega^n \tag{10}$$

where n is the frequency exponent in the range of ($0 < n < 1$). A and n are thermally activated quantities, hence electrical conduction is thermally activated process. σ_{DC} is limit value of $\sigma_{AC}(\omega)$ determined when $\omega \to 0$ and corresponds to DC conductivity value.

At low frequencies, where the applied electric field forces the charge carriers to drift over large distances, a tendency to retain almost constant values is recorded. When frequency is raised, the mean displacement of the charge carriers is reduced. After reaching the critical frequency ω_p, the real part of conductivity follows the law $\sigma_{AC} \sim \omega^n$ with $0 \leq n \leq 1$ characterizing hopping conduction. The term hopping refers to a sudden displacement of a charge carrier from one to another neighbouring position and in general includes both jumps over a potential barrier and quantum mechanical tunnelling [54,55].

The values of exponent n, σ_{AC}, and A were obtained by fitting Eq. 10 (σ_{AC} vs. ω) from 10^3 Hz to 10^5 Hz. The fit quality is usually evaluated by comparing the squared coefficient of linear correlation coefficient (R^2) obtained for each temperature (Table 2). The conduction mechanism in AC domain can be explained with the help of Correlated Barrier Hopping (CBH) model [56,57]. This model based on hopping of charge carriers over barrier predicts a value between 0 and 1 of the index n, hence this is consistent with the experimental results.

Using correlated barrier hopping (CBH) model [57], the binding energy was calculated according to the following equation:

$$\beta = \frac{6 \cdot k_B \cdot T}{W_m} \tag{11}$$

where $\beta = 1 - n$ and W_m is the binding energy, which is defined as energy required to remove charge carriers completely from one site to another site. W_m decreases with increasing Fe content in ZnO (Table 2). This result is in good agreement to the obtained band gap energy.

Using the values of the binding energy, minimum hopping distance R_{min} was calculated with equation 12 [58]:

$$R_{min} = \frac{2 \cdot e^2}{\pi \cdot \varepsilon \cdot \varepsilon_0 \cdot W_m} \tag{12}$$

where ε_0 is the permittivity of free space and ε is the dielectric constant. From the obtained results, it is seen that R_{min} increases with the increase in Fe^{3+} content in ZnO.

According to the Austin-Mott formula [59] based on the CBH model, AC conductivity $\sigma_{AC}(\omega)$ can be explained in terms of hopping of electrons between a pair of localized states $N(E_F)$ at the Fermi level. The conductivity σ_{AC} is related to the number of sites per unit energy per unit volume $N(E_F)$ at the Fermi level, as given by the following equation:

$$\sigma_{AC}(\omega) = \frac{\pi}{3} e^2 \omega k_B T (N(E_F))^2 \alpha^{-5} \left(\ln \frac{f_0}{\omega}\right)^2 \tag{13}$$

where e is the electronic charge, f_0 the photon frequency, and α is the localized wave function. The density of localized states $N(E_F)$ was calculated according to Eq. 13 assuming $f_0 = 10^{13}$ Hz, $\alpha = 10^{10}$ m^{-1}. Figure 11 illustrates the variation of $N(E_F)$ with frequency for the Fe-doped ZnO samples. It is observed that the obtained value of $N(E_F)$ increases with increasing Fe amount. This confirms increase of the electrical conductivity with increasing Fe content added to ZnO, and there is a growing concentration of defect energy states with increasing Fe content in ZnO [60].

3.6. Photocatalytic activity

In order to evaluate the photocatalytic performances of the as-prepared Fe-ZnO samples, the degradation of methylene blue (MB) in aqueous solution under UV

Table 2. The fitting parameters obtained from experimental data of conductivity as function frequency (σ_{AC} vs ω) using the Jonscher's power low and calculate values of W_m and R_{min}

Temperature [°C]	σ_{DC} [(Ω/cm)$^{-1}$]	A	n	R^2	W_m [eV]	R_{min} [nm]
ZnO	4.74×10^{-6}	7.31×10^{-8}	0.5487	0.9994	0.3415	2.47
$Zn_{0.98}Fe_{0.02}O$	5.38×10^{-6}	1.152×10^{-7}	0.5323	0.99965	0.3295	2.45
$Zn_{0.95}Fe_{0.05}O$	1.11×10^{-6}	0.4117×10^{-7}	0.4117	0.99993	0.2620	2.52

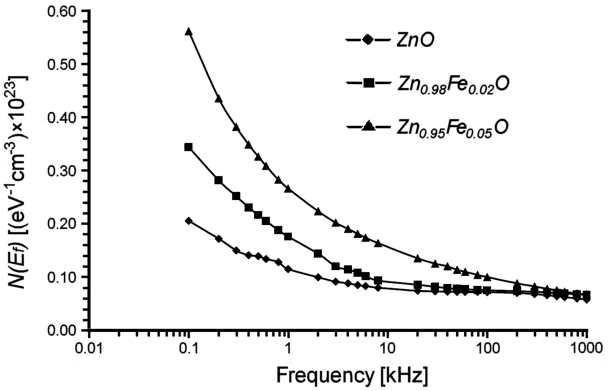

Figure 11. Variation of density state at Fermi level ($N(E_F)$) with frequency: a) ZnO, b) $Zn_{0.98}Fe_{0.02}O$ and c) $Zn_{0.95}Fe_{0.05}O$

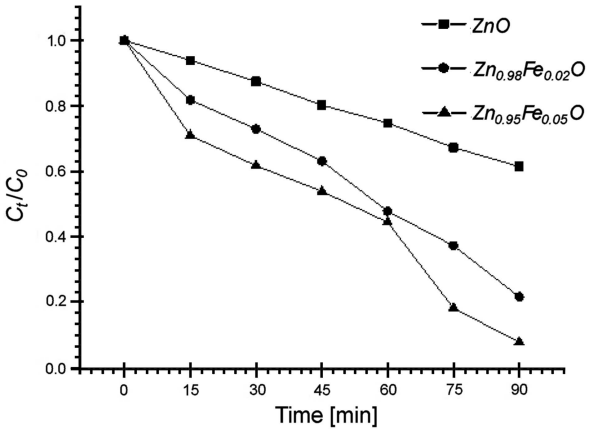

Figure 12. Photodegradation of MB by Fe-doped ZnO nanoparticles as a function of UV light irradiation time

light was investigated. Figure 12 shows the activities of the samples under UV light. All Fe-doped ZnO products display higher activities than that of the undoped ZnO, suggesting that Fe plays a positive role in the separation of photogenerated electron-hole pairs. Thus, the sample $Zn_{0.95}Fe_{0.05}O$ showed high degradation potential towards MB, i.e. it degrades 90% of BM in 90 min under UV light.

Figure 13 shows absorption spectra of MB solution treated at different times under UV irradiation treatment. The results reveal that the intensity of all MB peaks decrease with the treatment time increase without any new peaks appearing. It indicates that both catalysts can directly mineralize MB without any by-products. The insets in Fig. 13 display photographs of the MB solution decolouration under UV.

The obtained result is attributed to the fact that Fe ions can act as a photo-generated hole and trap, inhibiting the recombination of hole-electron [61]. As described by the schema in Fig. 14, and equations (inset in Fig. 14), the Fe^{3+} ions react as electron holes and traps which then form Fe^{2+} and Fe^{4+} (Eqs. 15 and 17). The Fe^{2+} and Fe^{4+} ions are relatively unstable compared with Fe^{3+} ions. To regain stability, these ions will react with oxygen and hydroxyl ions adsorbed onto the catalytic surface to produce hydroxyl ($OH^{\bullet}$) and superoxide O_2^- radicals (Eqs. 16 and 18).

IV. Conclusions

Pure and Fe-doped ZnO nanopowders were successfully synthesized via low cost sol gel method. Fine-scale and single phase wurtzite structure in all samples were confirmed by SEM and XRD, respectively. The observed energy gap of the Fe-doped ZnO decreased from 3.19 to 2.90 eV when Fe concentration is increased from 0 at.% to 5 at.%. In this region, more charge carriers are created by Fe-doping which induces the absorption and reduce the band gap. AC conductivity of the prepared samples increases with increase in frequency and complex impedance analysis showed single circular arc type behaviour, suggesting the dominance of grain resistance in all samples. The obtained results have been also discussed in terms of the correlated barrier hopping (CBH) model. The density of localized states $N(E_F)$ at the Fermi level and the binding energy W_m were calculated. W_m decreases with increasing Fe content in ZnO, which is in good agreement with the obtained band gap energy. It was observed that the obtained value of $N(E_F)$ increases with increasing Fe quantities. The Fe-doped ZnO products display higher activities than the pure ZnO, suggesting that Fe plays a positive role in the separation of photo-generated electron-hole pairs.

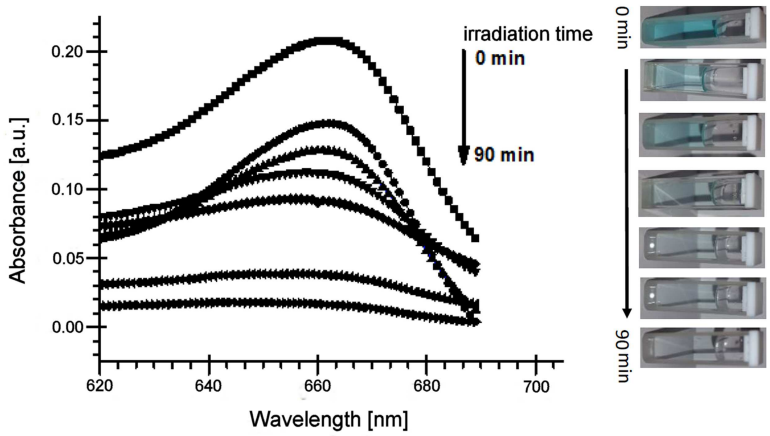

Figure 13. Absorption spectra of MB solution treated at different times under UV light

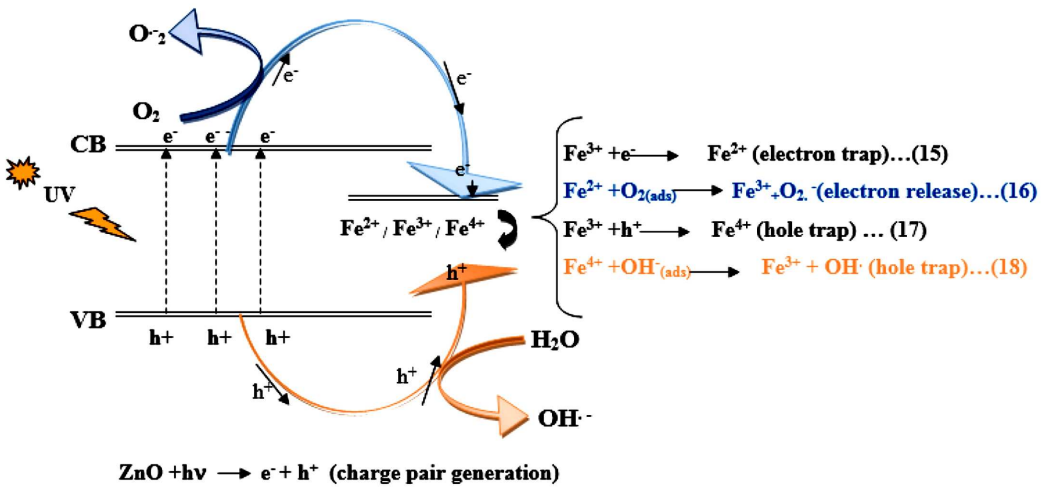

Figure 14. Schematic representation of photocatalytic processes for Fe-doped ZnO under UV irradiation

References

1. T.K. Gupta, "Application of zinc oxide varistors", *J. Am. Ceram. Soc.*, **73** (1990) 1817–1840.
2. Z. Zhou, K. Kato, T. Komaki, M, Yoshino, H. Yukawa, M. Morinaga, "Electrical conductivity of Cu-doped ZnO and its change with hydrogen implantation", *J. Am. Ceram. Soc.*, **24** (2004) 139–149.
3. J.H. Lim, C.K. Kang, K.K. Kim, I.K. Park, D.K. Hwang, S.J. Park, "UV electroluminescence emission from ZnO light-emitting diodes grown by high-temperature radiofrequency sputtering", *Adv. Mater.*, **18** (2006) 2720–2724.
4. D.M. Bagnall, Y.F. Chen, Z. Zhu, T. Yao, S. Koyama, M.Y. Shen, T. Goto, "Optically pumped lasing of ZnO at room temperature", *Appl. Phys. Lett.*, **70** (1997) 2230–2232.
5. G. Srinivasan, R.T. Rajendra Kumar, J. Kumar, "Li doped and undoped ZnO nanocrystalline thin films: a comparative study of structural and optical propertiese", *Opt. Mater.*, **30** (2007) 314–317.
6. S. Ilican, Y. Caglar, M. Caglar, F. Yakuphanoglu, "Electrical conductivity, optical and structural properties of indium-doped ZnO nanofiber thin film deposited by spray pyrolysis method", *Physica E*, **35** (2006) 131–138.
7. E. Fortunato, P. Barquinha, A. Pimentel, A. Goncalves, A. Marques, L. Pereira, R. Martins, "Recent advances in ZnO transparent thin film transistors", *Thin Solid Films*, **487** (2005) 205–211.
8. B.B. RAO, "Zinc oxide ceramic semi-conductor gas sensor for ethanol vapour", *Mater. Chem. Phys.*, **64** (2000) 62–65.
9. C. Liu, F. Yun, H. Morkoc, "Ferromagnetism of ZnO and GaN: A review", *Mater. Electron.*, **16** (2005) 555–597.
10. K. Matsubara, P. Fons, K. Iwata, A. Yamada, K. Sakurai, H. Tampo, S. Niki, "ZnO transparent conducting films deposited by pulsed laser deposition for solar cell applications", *Thin Solid Films*, **431** (2003) 16–21.
11. R. Tripathi, A. Kumar, C. Bharti, T.P. Sinha, "Dielectric relaxation of ZnO nanostructures synthesized by soft chemical method", *Curr. Appl. Phys.*, **10** (2010) 676–681.
12. D. Fernandez-Hevia, M. Peiteado, J. de Frutos, A.C. Caballero, J.F. Fernandez, "Wide range dielectric spectroscopy of ZnO based varistors as a function of sintering time", *J. Eur. Ceram. Soc.*, **24** (2004) 1205–1208.
13. T.A. Baeraky, "Microwave measurements of dielectric properties of zinc oxide at high temperature", *Egypt. J. Solids*, **30** (2007) 13–18.
14. Z. Dang, L. Fan, S. Zhao, C. Nan, "Dielectric properties and morphologies of composites filled with whisker and nanosized zinc oxide", *Mater. Res. Bull.*, **38** (2003) 499–507.
15. M. Ram, "A.c. conductivity and relaxation in $LiCoVO_4$ ceramics", *Curr. Appl. Phys.*, **10** (2010) 1013–1016.
16. A. Amine Khodjaa, T. Sehilia, J.-F. Pilichowskib, P. Bouleb. "Photocatalytic degradation of 2-phenylphenol on TiO_2 and ZnO in aqueous suspensions", *J. Photochem. Photobio. A: Chem.*, **141** (2001) 231–239.
17. B. Dindar, S. Içli, "Unusual photoreactivity of zinc oxide irradiated by concentrated sunlight", *J. Photochem. Photobio. A: Chem.*, **140** (2001) P 263–268.
18. C. Panatarani, I.W. Lenggoro, K. Okuyama, "The crystallinity and the photoluminescent properties of spray pyrolyzed ZnO phosphor containing Eu^{2+} and Eu^{3+} ions", *J. Phys. Chem. Solids*, **65** (2004) 1843–1847.
19. Y.S. Wang, P.J. Thomas, P. O'Brien, "Nanocrystalline ZnO with ultraviolet luminescence", *J. Phys. Chem. B*, **110** (2006) 4099–4104.
20. A. Sajid Ali, N. Ambreen, F. Bushara, W. Khan, A.H. Naqvi, "Investigation on structural, optical and dielectric properties of Co doped ZnO nanoparticles synthesized by gel-combustion route", *Mater. Sci.*

Eng. B, **177** (2012) 428–435.
21. I. Khan, S. Khan, R. Nongjai, H. Ahmed, W. Khan, "Structural and optical properties of gel-combustion synthesized Zr doped ZnO nanoparticles", *Opt. Mater.*, **35** (2013) 1189–1193.
22. T.V. Vimalkumar, N. Poornima, C. Sudha Kartha, K.P. Vijayakumar, "Effect of precursor medium on structural, electrical and optical properties of sprayed polycrystalline ZnO thin films", *Mater. Sci. Eng. B*, **175** (2010) 29–35.
23. F. Ahmed, S. Kumar, N. Arshi, M.S. Anwar, S.N. Heo, B.H. Koo, "Doping effects of Co^{2+} ions on structural and magnetic properties of ZnO nanoparticles", *Acta Mater.*, **60** (2012) 5190–5196.
24. W. Huang, X. Tanga, I. Felnerb, Y. Koltypin, A. Gedanken, "Preparation and characterization of Fe_xO_y–TiO_2 via sonochemical synthesis", *Mater. Res. Bul.*, **37** (2002) 1721–1735.
25. C.R. Estrellan, C. Salim, H. Hinode, "Photocatalytic activity of sol-gel derived TiO_2 co-doped with iron and niobium", *React. Kinet. Catal. Lett.*, **98** (2009) 187–192.
26. D.K. Shukla, S. Mollah, "dc conductivity and dielectric properties of V_2O_5-Bi_2O_3-ZnO glass", *Indian J. Pure Appl. Phys.*, **45** (2007) 52–56.
27. V.H. Mudavakkat, M. Noor-A-Alam, K. Kamala Bharathi, S. AlFaify, A. Dissanayake, A. Kayani, C.V. Ramana, "Structure and AC conductivity of nanocrystalline yttrium oxide thin films", *Thin Solid Films*, **519** (2011) 7947–7950.
28. H. El Mkami, B. Deroide, R. Backov, J.V. Zanchetta, "dc and ac conductivity of $(V_2O_5)_x(B_2O_3)_{1-x}$ oxide glasses", *J. Phys. Chem. Solids*, **61** (2000) 819–826.
29. P. Sahay, S. Tewari, R. Nath, S. Jha, M. Shamsuddin, "Studies on ac response of zinc oxide pellets", *J. Mater. Sci.*, **43** [13] (2008) 4534–4540.
30. J. Jose, M. Abdul Khadar, "Role of grain boundaries on the electrical conductivity of nanophase zinc oxide", *Mater. Sci. Eng. A*, **304** (2001) 810–813.
31. J.R. Macdonald, "Impedance spectroscopy", *Ann. Biomed. Eng.*, **20** (1992) 289–305.
32. P. Knauth, J. Schoonman, "Defect and transport properties of nanocrystalline ceramics and thin films", *Electron. Mater.: Sci. Technol.*, **7** (2002) 111–131.
33. A.K. Zak, W.H.A. Majid, M. Darroudi, R. Yousefi "Synthèse et caractérisation des nanoparticules de ZnO préparent Dans Les Médias de gelatine", *Lettres Matériaux*, **65** [1] (2011) 70–73.
34. A. Khorsand Zak, W.H. Abd. Majid, M. Mahmoudian, "Starch-stabilized synthesis of ZnO nanopowders at low temperature and optical properties study", *Adv. Powder Technol.*, **24** [3] (2013) 618–624.
35. B.A.M. Muneer, K.H. Abdul Amir, M. Abubakar, T.S. Mohd, S. Kamaruzzaman,, "Visible light photocatalytic activity of Fe^{3+}-doped ZnO nanoparticle prepared via sol-gel technique", *Chemosphere*, **91** (2013)1604–1611.
36. H. Liu, J. Yang, Y. Zhang, L. Yang, M. Wei, X. Ding, "Structure and magnetic properties of Fe-doped ZnO prepared by the sol-gel method", *J. Phys.: Condens. Matter.*, **21** (2009) 145803–145807.
37. R. Saleh, S.P. Prakoso, A. Fishli, "The influence of Fe doping on the structural, magnetic and optical properties of nanocrystalline ZnO particles", *J. Magn. Magn. Mater.*, **324** (2012) 665–670.
38. A.K. Srivastava, M. Deepa, N. Bahadur, M.S. Goyat, "Influence of Fe doping on nanostructures and photoluminescence of sol-gel derived ZnO", *Mater. Chem. Phys.*, **114** (2009) 194–198.
39. W. Cheng, X. Ma, "Structural, optical and magnetic properties of Fe-doped ZnO", *J. Phys.: Conf. Ser.*, **152** (2009) 012039.
40. B.D. Cullity, S.R. Stock, *Elements of X-Ray Diffraction*, 3rd ed., Prentice Hall, USA, 2001.
41. P.K. Manoj, V.K. Benny Joseph, D. Vaidyan, D.A. Sumangala, "Preparation and characterization of indium-doped tin oxide thin films", *Ceram. Int.*, **33** (2007) 273–278.
42. S. Fujita, K. Kaneko, "Epitaxial growth of corundum-structured wide band gap III-oxide semiconductor thin films", *J. Crystal Growth*, **401** (2014) 588–592.
43. S.J. Chen, J.G. Ma, D.X. Zhao, Z.Z. Zhi, Y.M. Lu, J.Y. Zhang, D.Z. Shen, X.W. Fa, "High-quality ZnO thin films prepared by two-step thermal oxidation of the metallic Zn", *J. Crystal Growth*, **240** (2002) 467–472.
44. J. Robertson, "Band offsets of wide-band-gap oxides and implications for future electronic devices", *J. Vac. Sci. Technol. B*, **18** (2000) 1785–1791.
45. R.B. Bylsma, W.M. Becker, J. Kossut, U. Debska, D. Yoder-Short, "Dependence of energy gap on x and T in $Zn_{1-x}Mn_xSe$: The role of exchange interaction", *Phys. Rev. B*, **33** (1986) 8207–8215.
46. S. Nilavazhagan, S. Muthukumaran, M. Ashokkumar, "Reduction of sodium strengths in wastewater streams from food and beverage industries", *J. Mater. Sci.: Mater. Electron.*, **24** (2013) 2581–2592.
47. K. Samanta, P. Bhattacharya, R. Katiyar, "Microstructural and ferromagnetic properties of ZnO thin films", *J. Appl. Phys.*, **105** (2009) 113929.
48. C. Koops, "On the dispersion of resistivity and dielectric constant of some semiconductors at audiofrequencies", *Phys. Rev.*, **83** [1] (1951) 121–124.
49. K.W. Wagner, "Zur theorie der unvollkommenen dielektrika", *Annalen der Physik*, **345** [5] (1913) 817–855.
50. F. Kröger, H. Vink, "Relations between the concentrations of imperfections in crystalline solids", *Solid State Phys.*, **3** (1956) 307–435.
51. D.L. Sidebottom, "Universal approach for scaling the ac conductivity in ionic glasses", *Phys. Rev. Lett.*, **83** [5] (1999) 3653–3656.
52. B. Roling, A. Happe, K. Funke, M.D. Ingram, "Carrier concentrations and relaxation spectroscopy: new

information from scaling properties of conductivity spectra in ionically conducting glasses", *Phys. Rev. Lett.*, **78** [11] (1997) 2160–2163.
53. S. Capaccioli, M. Lucchesi, P.A. Rolla, G. Ruggeri, "Dielectric response analysis of a conducting polymer dominated by the hopping charge transport", *J. Phys.: Condens. Matter*, **10** (1998) 5595.
54. A.K. Jonscher, "The 'universal' dielectric response", *Nature*, **267** (1977) 673.
55. H. Böttger, U.V. Bryskin, *Hoping Conduction in Solids*, Verlag Akademie, Berlin, Vol. 41, (1985) pp. 169–213.
56. S.R. Eilliot, "Temperature dependence of ac. conductivity", *Philos. Mag. B*, **37** (1978) 553–560.
57. S. Mollah, K.K. Som, K. Bose, B.K. Chaudri, "ac conductivity in $Bi_4Sr_3Ca_3Cu_yO_x$ (y = 0–5) and $Bi_4Sr_3Ca_{3-z}Li_zCu_4O_x$ (z = 0.1–1.0) semiconducting oxide glasses", *J. Appl. Phys.*, **74** (1993) 931–937.
58. R. Salam, "Trapping parameters of electronic defects states in indium tin oxide from AC conductivity", *Phys. Status Solidi A*, **117** (1990) 535–540.
59. I.G. Austin, N.F. Mott, "Polarons in crystalline and non-crystalline materials", *Adv. Phys.*, **18** (1969) 41–102.
60. N.Ch. Ramesh Babu, M.A. Valente, N. Narasimha Rao, M.P.F. Graça, G. Naga Raju, M. Piasecki, I.V. Kityk, N. Veeraiah, "Low temperature dielectric dispersion and electrical conductivity studies on Fe_2O_3 mixed lithium yttrium silicate glasses", *J. Non-Crystalline Solids*, **358** (2012) 3175–3186.
61. M.H. Zhou, J.G. Yu, B. Cheng, H.G. Yu, "Preparation, photocatalytic activity of Fe-doped mesoporous titanium dioxide nanocrystalline photocatalysts", *Mater. Chem. Phys.*, **93** (2005) 159–163.